ICAS 2021 SHANG HAI
International Council of the Aeronautical Sciences
32nd Congress of the International Council of the Aeronautical Sciences
September 6-10, 2021
Pudong Shangri-La, Shanghai, China

ROBUST DESIGN OF 3D SHOCK CONTROL BUMPS TO TRANSPORT AIRCRAFT UNDER REALISTIC UNCERTAINTIES

Christian Sabater[1] & Stefan Goertz[2]

[1]German Aerospace Center, DLR

Abstract

With the continuous increase in the number of commercial flights, environmental and economic concerns are key drivers towards the reduction of aircraft operational cost and emission of greenhouse gasses. The use of aerodynamic shape optimization, regularly carried out in a deterministic fashion, plays a key role in reducing aerodynamic drag and the overall carbon footprint. However, the sensitivity of the optimum shape to operational and environmental uncertainties can affect the real aircraft performance. A possible solution to increase the robustness of existing aircraft is the development of retrofits that are tailored to the current airliner's operations. Shock control bumps are attractive retrofit for aircraft flying in routes at considerably higher speeds than the design point. The objective of this paper is the robust design of a 3D array of shock control bumps that can be retrofitted to the XRF1 transport aircraft configuration. Realistic uncertainties in Mach number, lift coefficient and altitude are extracted following aircraft surveillance data using the OpenSky Network for a selected flight route. A tailored Gradient-Based Robust Design methodology that combines the adjoint method with Gaussian Processes is used for the optimization under these uncertainties. The robust optimum array of bumps is able to mitigate the normal shock wave over the upper surface of the wing, reducing the average drag by 3.2% compared to the clean wing. More importantly, its performance is superior compared to the configurations obtained at single-point and multi-point optimization, showcasing the benefits of a probabilistic formulation for the retrofit of 3D shock control bumps.

Keywords: Gradient-Based Robust Optimization, Shock Control Bumps, Aerodynamics, Uncertainty Quantification, Robust Design

1. Introduction

With the continuous growth of commercial aviation, environmental and economic concerns are key drivers towards the reduction of operational costs and emission of greenhouse gasses [1]. The aerodynamic design of transonic wings is already a mature field, and the use of aerodynamic shape optimization is a well established discipline in industrial setting [2]. However, aircraft manufacturers design configurations taking into account a representative but limited set of flight conditions. The cruise point is chosen to simplify and have more control of the design process. Even a multi-point approach [3, 4] does not truly represent reality, as still, only a discrete combination of flight conditions are looked upon. State of the art work focuses on the optimization under a large number of discrete mission points such as [5], with focus on payload and range, or by the minimization of the average value [6], where the flight conditions (in this case Mach and lift coefficient) are approximated to normal distributions according to quadrature methods.

In practice, airlines do not always fly at the conditions they were designed to operate. They are affected by operational requirements and environmental uncertainties. The cost index, the ratio between time and fuel-related costs [7], also plays a key role in determining the aircraft speed. As a result, Reynolds number Re, Mach number M and lift coefficient C_L, three of the most important parameters when performing aerodynamic design, can not be treated as single deterministic values in the optimization process. A full probabilistic approach is required to better simulate the real performance of the aircraft. On the one hand, the aircraft true airspeed (and consequently the Mach number) is affected by several factors such as scheduling, wind and other environmental uncertainties. Pilots may decide to fly at (slightly) higher Mach numbers if they are late or under unexpected headwind (and thus a reduced ground speed), or at reduced speeds it in case they have tail wind or decide

to save fuel, in relation with the cost index [7]. On the other hand, the aircraft operational weight is one of the most difficult parameters to predict. Despite an initial estimation can be given for the take-off weight according to the aircraft empty weight and fuel, several factors can strongly influence it such as passengers and cargo weight or estimation of fuel density (even a small shift can lead towards a big change in weight). In addition, weight is constantly changing during the flight, as is dependent of the aircraft aerodynamic efficiency and specific fuel consumption of the engines. As a result, when flying at constant altitude the lift coefficient is continuously decreasing. Aircraft can not always fly at the optimal altitude for a given weight, and sometimes need to wait more than expected to get ATC clearance to climb at higher flight levels, influencing fuel consumption.

These changes in operational conditions leads towards the deterioration of the average performance compared to the predicted when it was designed using deterministic methods. The ideal solution would be to robustly design the whole aircraft taking into account a probabilistic approach of these uncertainties beforehand. However, this is not always possible. OEM's can not predict how a new aircraft will be operated, as ATC regulations and airliners requirements are constantly changing. Following the same reasoning, airlines may decide to change their operations according to the improved performance of a novel configuration. As a result, a chicken-egg situation is created in which OEM's are unable to anticipate the operational behaviour of their costumers, and airliners can not adapt beforehand their operations.

A possible solution to increase robustness of existing aircraft is the development of retrofits that are tailored to the current airliner's operations. These devices in theory could be added to a current fleet at relatively low cost, improving the average performance compared to situations in which no retrofit is added. An attractive retrofit would be the addition of shock control bumps for aircraft flying in routes at considerably higher speeds than the ones they were designed from. When aircraft fly faster or with a higher lift coefficient, stronger shock waves are present over the upper surface of the wing, increasing wave drag. This increase in drag can be mitigated by robustly designing tailored shock control bumps that could isentropically decelerate the flow [8]. For simplicity, the shock control bumps can be fixed devices placed over the upper surface of the wing [9]. As these would be tailored for the aircraft operations (e.g. designed specifically for given route), an adaptation of the bump in flight would not be necessary saving in installation costs and complexity of a moving mechanism. In overall, a wing with a robustly designed array of shock control bumps would outperform the average performance of the same clean wing at cruise conditions.

Shock Control bumps were first introduced in 1992 for the mitigation of wave drag [10]. Further studies took place in Europe within the EUROSHOCK II project [11] and in the USA [12] to investigate its full potential. From the 2000s, the focus has been on understanding the flow physics [13] and the realization of optimization studies [14], [15]. A complete overview of Shock Control Bumps is given in [16]. A crucial aspect that is gaining more attention recently is the need for a robust SCB configuration for industrial applications [17], [18]. The robustness of shock control bumps, i.e., its ability to effectively reduce wave drag at different flight conditions, is of primary concern as they are highly sensitive to the shock wave location [16]. At freestream velocities or lift coefficients different from their design point, SCBs suffer from adverse effects as the shock wave is not located in the designed location [8]. For example, when the shock wave moves upstream (due to a decrease in flight speed or lift coefficient), the flow is re-accelerated due to the curvature of the bump, leading to a second supersonic region behind the first shock. On the contrary, if the shock is located downstream of the SCB, no lambda shock structure is generated and the flow is further, leading to an increased shock strength and possibly causing flow separation. As a result, efficient robust optimization techniques can cope with the realistic design of SCBs by accounting for the uncertainties during the design stage [19].

The objective of this paper is the efficient robust design of shock control bumps for a transonic aircraft in order to improve the average performance of a fleet under realistic operational uncertainties. Up to now, three main limitations made not possible the robust design and retrofit of aerodynamic components: the lack of efficient robust design frameworks able to deal with expensive CFD simulations, the lack of public data regarding aircraft operations to characterize uncertainties and the lack of realistic test cases and applications that could be used for the robust formulation. Each of this limitations will be overcomed in the present paper. A robust design framework that uses and adjoint formulation in combination with Gaussian Processes will be introduced in Section 2. . In Section 3.the XRF1 research aircraft configuration will be introduced, together with novel parametrization of an array of shock control bumps to be retrofitted over the upper surface of the wing. In Section 4.aircraft surveillance data will be used to investigate operational uncertainties, with special focus on flight speed. Finally, the robust optimization results will be introduced in Section 5.and compared with those obtained using deterministic

optimization, demonstrating the need of a probabilistic approach.

2. Robust Design Framework

This section presents the optimization under uncertainty framework used to efficiently obtain the optimum configuration. The exact details of the framework can be found in [20].

2.1 Problem Definition

The classical deterministic optimization problem is defined through the optimization of the aircraft drag coefficient C_D, depending on the design variables $\boldsymbol{x}$ at given operational conditions, $\boldsymbol{A}$

$$J^*(\boldsymbol{x}^*) = \min_{\boldsymbol{x}} \{C_D(\boldsymbol{x}, \boldsymbol{A})\} \tag{1}$$

To reduce the sensitivity of the drag against the operating conditions, the multi-point optimization can be chosen. The minimization consists on a weighted average of the C_D evaluated at n_m flight conditions:

$$J^*(x^*) = \min_{\boldsymbol{x}} \left\{ \sum_{j=1}^{n_m} w_j C_D(\boldsymbol{x}, \boldsymbol{A_j}) \right\} \tag{2}$$

However, the weights are usually selected according to expert knowledge and the optimum configuration is strongly dependent on the selected flight conditions.

The robust optimization involves the presence of uncertainties $\boldsymbol{\xi}$ either in operational conditions, geometry, or both. As a result, the C_D becomes a random variable and the problem is shifted towards the optimization of an statistic of the C_D. In this case, a robust design approach is defined by minimizing the average drag, μ_{C_D} (mean) and variability σ_{C_D} (standard deviation).

$$J^*(\boldsymbol{x}^*, \boldsymbol{\xi}) = \min_{\boldsymbol{x}} \left\{ w_\mu \mu_{C_D}(\boldsymbol{x}, \boldsymbol{\xi}) + w_\sigma \sigma_{C_D}(\boldsymbol{x}, \boldsymbol{\xi}) \right\} \tag{3}$$

By changing the weights, it is possible to come up with different configurations with focus on variability, expectation or both.

2.2 Gradient-Based Optimization

Gradient-based aerodynamic shape optimization is a mature technology [21, 22] as it is able to handle hundreds of design parameters, the relatively fast convergence towards an optima and the possibility of obtaining gradients through an adjoint formulation. Following equation (1), from an initial sample $\boldsymbol{x_i}$, the optimum solution can be found through an iterative process where the next step $\boldsymbol{x_{i+1}}$ is found by:

$$\boldsymbol{x_{i+1}} = \boldsymbol{x_i} + h \nabla J \tag{4}$$

where ∇ is the gradient (search direction) of the objective function J, and h is the step size along the search dimension. The use of an adjoint formulation [23] enables the calculation of sensitivities at a cost independent on the number of design parameters, in opposition to finite differences. This is especially suitable when the number of cost functions is relatively small compared to the number of design parameters. However, gradient-based optimization can only lead to a local optimum and its solution is dependent on the initial starting location, $\boldsymbol{x_1}$.

Under uncertainty, the objective function becomes a random variable. Following the minimization of mean and standard deviation in equation (3), from a given sample $\boldsymbol{x_i}$, the next one $\boldsymbol{x_{i+1}}$, is found by:

$$\boldsymbol{x_{i+1}} = \boldsymbol{x_i} + h \nabla J(\boldsymbol{x_i}) = \boldsymbol{x_i} + h \left[w_\mu \nabla \mu_{C_D}(\boldsymbol{x_i}) + w_\sigma \nabla \sigma_{C_D}(\boldsymbol{x_i}) \right] \tag{5}$$

The statistical moments of the C_D, $\mu_{C_D}(\boldsymbol{x})$, $\sigma_{C_D}(\boldsymbol{x})$ and its derivatives, $\nabla \mu_{C_D}(\boldsymbol{x})$, $\nabla \sigma_{C_D}(\boldsymbol{x})$, are required for the gradient based optimization.

2.3 Obtaining the Gradients of the Statistics

At a given design point, $\boldsymbol{x_i}$, the deterministic gradients of the C_D with respect to the design parameters at realizations $\boldsymbol{\xi_j}$, $j = 1 \dots n_\xi$ are usually available using an adjoint formulation: $\nabla Y\left(\boldsymbol{x_i}, \boldsymbol{\xi_j}\right)$. From these, the gradient of the mean value at the design point $\nabla \mu_Y(\boldsymbol{x_i}) = \left\{ \frac{d\mu}{dx^1}\Big|_{\boldsymbol{x_i}}, \frac{d\mu}{dx^2}\Big|_{\boldsymbol{x_i}} \dots \frac{d\mu}{dx^{dx}}\Big|_{\boldsymbol{x_i}} \right\}^T$ are derived. The derivative of the mean value of the C_D with respect to a given design parameter x^k at any given design point $\boldsymbol{x}_i$, $\frac{d\mu_{C_D}}{dx^k}\Big|_{\boldsymbol{x_i}}$, is obtained from:

$$\frac{d\mu_{C_D}}{dx^k}\Big|_{\boldsymbol{x}_i} = \frac{1}{n_\xi} \sum_{j=1}^{n_\xi} \frac{dC_D}{dx^k}\Big|_{\boldsymbol{x_i}, \boldsymbol{\xi_j}} \tag{6}$$

Where $\frac{dC_D}{dx^k}\Big|_{\boldsymbol{x_i}, \boldsymbol{\xi_j}}$ are realizations of the derivative at n_ξ different uncertain locations $\boldsymbol{\xi_j}$ at the design point $\boldsymbol{x_i}$. These derivatives are computed non-intrusively using an adjoint computation.
The derivative of the standard deviation of the C_D respect to each design parameter also is also found analytically:

$$\frac{d\sigma_{C_D}}{dx^k}\Big|_{\boldsymbol{x_i}} = \frac{1}{n_\xi\, \sigma_{C_D}(\boldsymbol{x_i})} \sum_{j=1}^{n_\xi} \left(Y\left(\boldsymbol{x}_i, \boldsymbol{\xi_j}\right) - \mu_{C_D}(\boldsymbol{x}_i) \right) \left(\frac{dC_D}{dx^k}\Big|_{\boldsymbol{x_i}, \boldsymbol{\xi_j}} - \frac{d\mu_{C_D}}{dx^k}\Big|_{\boldsymbol{x}_i} \right)^2 \tag{7}$$

This formulation is generic and only requires a large number of samples, n_ξ, evaluated in the full order model.

2.4 Surrogate Based Uncertainty Quantification

The main problem of uncertainty quantification is the large number of function evaluations required to propagate the uncertainty of the input parameters (in this case operational conditions) to the C_D at any given design, $\boldsymbol{x}_j$ [24]. To directly perform Monte Carlo Simulations is prohibitive when using CFD solvers. A typical approach is then the use of surrogates of the stochastic space for example, through Polynomial Chaos Expansion or Gaussian Processes Regression (GPR).
GPR models have been traditionally used in aerodynamic shape optimization as surrogate models for global optimization [25]. However, these have been recently used as non-intrusive approach to perform uncertainty quantification due to its good capability to globally represent the stochastic space [19, 26].
The main idea of UQ in Gaussian Processes is as follows: at a given configuration, $\boldsymbol{x_i}$, an initial design of experiments (DoE) sampling in the stochastic space (in this case random operating conditions), is evaluated in the full order model. Based on this sampling, the GP is built. Then, a large number (n_ξ) of Quasi Monte Carlo samples can be cheaply evaluated in the surrogate to obtain the statistic, such as the mean or standard deviation of the drag, following equation 8,

$$\mu_{C_D}(\boldsymbol{x_i}) = \frac{1}{n_\xi} \sum_{k=1}^{n_\xi} \hat{C_D}\left(\boldsymbol{x}_j, \boldsymbol{\xi}_k\right) \qquad \sigma_{C_D}(\boldsymbol{x_i}) = \sqrt{\frac{1}{n_\xi} \sum_{k=1}^{n_\xi} \left[\hat{C_D}\left(\boldsymbol{x}_j, \boldsymbol{\xi}_k\right) - \mu_{C_D}\right]^2} \tag{8}$$

where $\hat{C_D}\left(\boldsymbol{x}_j, \boldsymbol{\xi}_k\right)$ is obtained by prediction of the surrogate built in the stochastic space $\boldsymbol{\xi}$. The Gaussian Process model consists of Universal Kriging with a Gaussian Kernel (exponent fixed to 2). They hyperparameters of the correlation model are tuned according to the maximization of the model likelihood through Differential Evolution. The Surrogate-Modelling for Aero-Data Toolbox (SMARTy) developed by DLR is used for the initial Design of Experiments sampling and for the creation of the Kriging surrogate [27].
To increase the accuracy of the statistics, after the DoE, an active infill criteria that deals with sampling evenly in the stochastic space [28] is used. Gaussian Processes provide the estimation of the surrogate error at any given point in the stochastic space, $\hat{s}(\boldsymbol{\xi})$ [25]. Then, new samples are added in the location $\boldsymbol{\xi}_k^*$ where the product of the probability distribution function of the input parameters, PDF_X times the error estimation of the error is maximized. The optimum location is found in the surrogate through Differential Evolution. Additional details of the methodology can be found in [19]

2.5 Optimization Architecture

The optimization framework, firstly introduced in [20], combines the gradients obtained by the adjoint formulation with the uncertainty quantification using GPR. As shown in Figure 1, this consists of two levels: the gradient based optimizer in the outer level, and the SBUQ framework in the inner one. A Sequential Least SQuares Programming (SLSQP) [29] is selected as optimizer. At any given design point, $\boldsymbol{x}_i$, the optimizer requires both the statistic (blue dot), such as the mean, $\mu(\boldsymbol{x})$, and its gradients (green arrows) $\nabla\mu(\boldsymbol{x_i})$ w.r.t. the design parameters. The SBUQ is not only used to obtain the statistics, but also the gradients. As a result, a surrogate model of the gradients is constructed per each design parameter x^k to accurately obtain the gradients of the statistics.

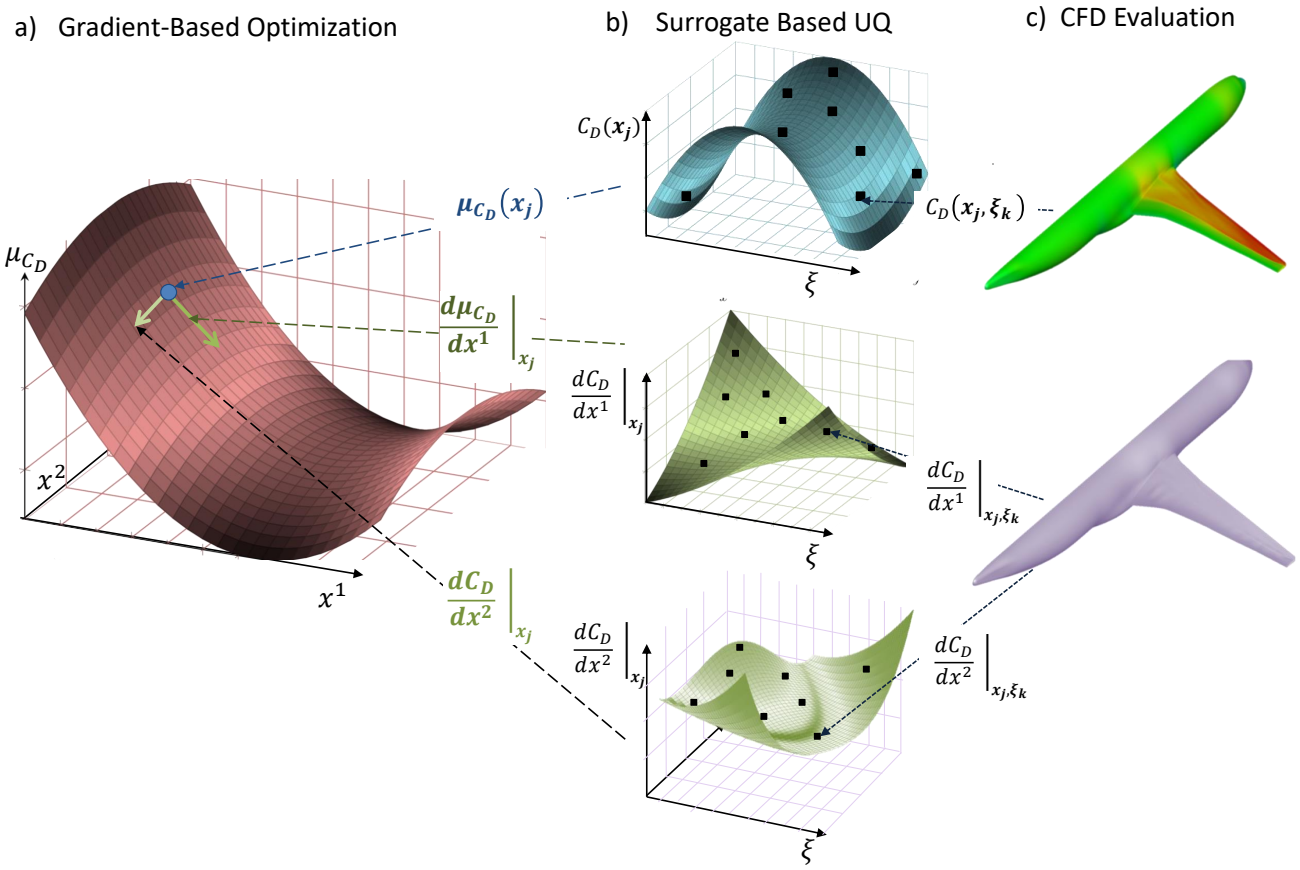

Figure 1 – Robust Design Framework using the Adjoint and Gaussian Process [20]: a) Gradient Based Optimization of the mean; b) Uncertainty Quantification through Gaussian Processes of the C_D and each of its gradients; c) Evaluation of each deterministic solution in full order model

3. Definition of Test Case

The following section introduces the configuration used as test case, the numerical model and a suitable parametrization for the retrofit of shock control bumps.

3.1 XRF1 Configuration

For a realistic representation of commercial transport aircraft, the Airbus XRF1 research aircraft is selected as test case. Resembling the Airbus A330, the XRF1 is a generic wide-body, twin-engine configuration for long-range missions that is designed to carry around 350 passengers. The configuration is provided by Airbus as a platform for research with external partners on the development and demonstration of relevant capabilities. It has been used in the past in several European and DLR projects. For the demonstration of the capabilities of shock control bumps, only the wing-body configuration is considered as it is representative enough of the aerodynamic features of transonic flow. The mesh and surface pressure coefficient are shown in Figure 2.

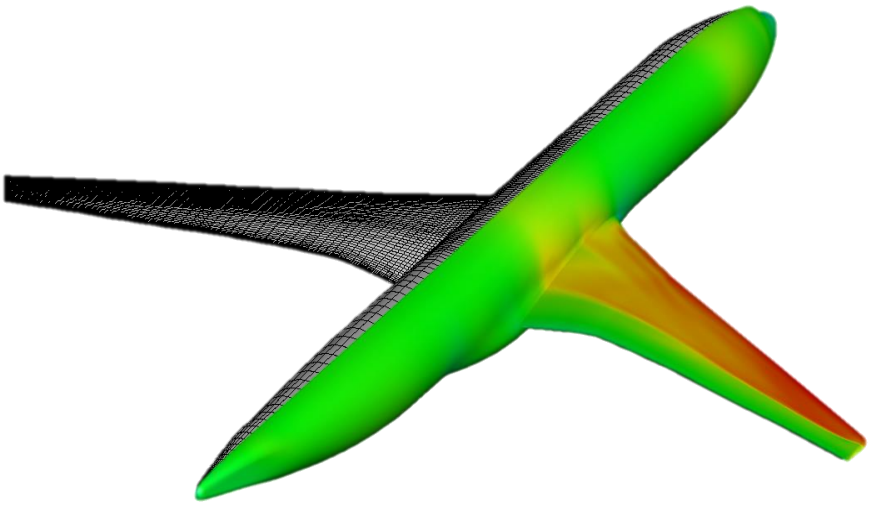

Figure 2 – Numerical mesh(left) and pressure coefficient distribution (right) of XRF1 configuration

3.2 Numerical Model

To obtain the aerodynamic performance of the XRF1, the high-fidelity DLR flow solver TAU [30] is executed on an HPC cluster system using DLR's FlowSimulator Data Manager (FSDM) environment. The Reynolds Average Navier Stokes (RANS) equations are solved using the Spalart-Allmaras turbulence model. The solution is converged when the density residual is lower than 1e-7. A mesh deformation tool developed by DLR using linear elasticity theory [31] is used to change the geometry at any given design vector.

3.3 Parametrization of Shock Control Bumps

Two different alternatives can be chosen for the design of shock control bumps: a continuous extruded 3D bump and a set of multiple bumps. The later is preferred as ease of manufacture and integration, despite the former can eventually lead to better performance due to the possibility of increasing the parametrization.
An array of individual shock control bumps is placed over the upper surface of the wing as shown in Figure 3. The cross section at the center of each bump is defined by means of a Hicks-Henne Sinusoidal Function with 5 design parameters for each bump, following the 2D parametrization of Mazaheri [32] and Tian [33].

$$z(x) = h_{bump}\left[\sin\left(\pi\left(\frac{x-x_{start}}{l_{bump}}\right)^{m}\right)\right]^{t_{bump}}, \qquad x_{start} \leq x \leq x_{start}+l_{bump} \tag{9}$$

where m is used to modify the asymmetry of the bump:

$$m = \frac{\log(0.5)}{\log\left(x_{h_{bump}}\right)} \tag{10}$$

The slope of the curvature of this function is zero at both ends. As a result, no discontinuities are present between the bump and the airfoil. A second advantage with respect to other parametrization such as NURBS curves is that the Hicks-Henne parameters represent the physical geometry of the bump, allowing for a straightforward definition of the design space as shown in Table 1. The parameters are normalized according to the airfoil chord length, c. The 3D geometry is achieved by extruding the 2D bump spanwise along the wingspan, allowing for a smooth bump. As a result, the width, w_i and the lateral location y of each bump are also design parameters, with the constraint that no overlapping bumps can exist. This flexible parametrization is able to handle an arbitrary number of bumps. However, to avoid dealing with a mixed-integer problem, the number of bumps is fixed beforehand for each optimization.
The bounds of the parameters have been chosen according to physical constraints in order to reach a realistic design. For example, a bump height of 0 is equivalent to the baseline configuration of the wing with no bump. The upper limit of $0.015c$ is chosen having into account that the order of magnitude of the bump height is strongly related to the boundary layer displacement thickness. The location of the bump is centred along the shock wave location of the initial wing.

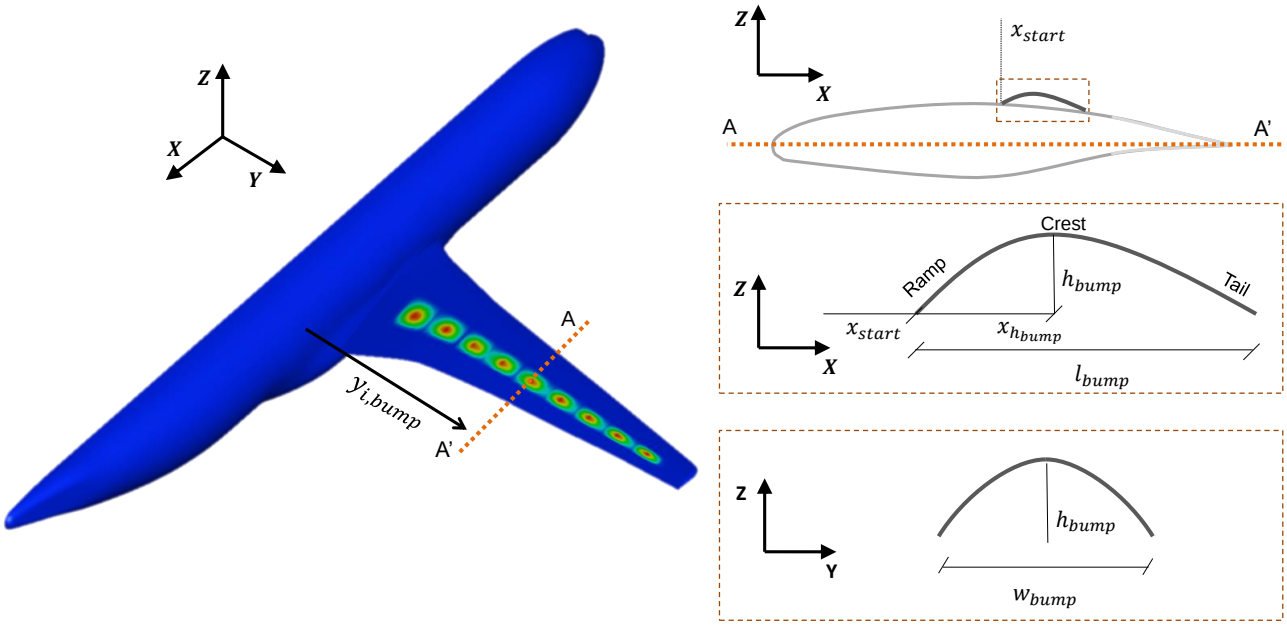

Figure 3 – Parametrization of an array of shock control bumps over a 3D wing

Table 1 – Design parameters for each shock control bump

Parameter	Description	Lower Bound	Upper Bound
h_{bump}/c	Bump maximum height	0	0.015
$x_{h_{bump}}/c$	Bump maximum height location	0.4	0.85
l_{bump}/c	Bump length	0.15	0.45
x_{start}/c	Bump starting location	0.3	0.54
t_{bump}	Bump slope factor	0.2	0
$w_{bump}/w_{bump,max}$	Bump width	0.0	1
$y_{bump}/y_{bump,0}$	Bump Lateral displacement	0.	1

3.4 Deterministic Cruise Point

The cruise point is referred as the "deterministic" flight condition as no uncertainties are present. In this case, the XRF1 operating point is chosen as freestream Mach number $M = 0.83$, flight level FL=380, and lift coefficient $C_L = 0.5$, following [34]. The angle of attach is changed iteratively during the flow solution in order to match the required lift. Assuming a standard atmosphere [35], the freestream pressure, density, and Reynolds number can be obtained.

4. Parametrization of Uncertainties: OpenSky Data

The main objective of this section is to come up with a representative dataset of operational uncertainties for the XRF1 configuration, that can be directly used when performing CFD simulations. The freestream Mach number, the lift coefficient and the aircraft altitude are the chosen parameters.

To understand the variability in operating conditions of a representative fleet of aircraft, data from the OpenSky network is gathered. The OpenSky Network is a community-based receiver network that collects real-world air traffic data through the Automatic Dependent Surveillance Broadcast ADS-B and Mode S technologies [36]. These provide detailed aircraft information over the publicly accessible 1090 MHz radio frequency channel. In opposition to commercial services available in the Internet that include radar visualization, OpenSky gathers the raw data and makes it accessible to researchers.

4.1 Gathering and Analysing Operational Data

The key indicators in this analysis are the aircraft true speed (TAS), Mach number and aircraft altitude. These datasets are provided almost at every second by the interrogation of the Mode S secondary surveillance radar. In particular, the Comm-B Data selection (BDS) codes, provides information to ATC regarding callsign, communication capabilities and aircraft flight states. The raw data can be received with a simple ground receiver, and is stored by OpenSky in a database. This can be easily decoded to obtain not only aircraft speeds, but also meteorological information, turn rates and aircraft intent among others. For more information regarding the extraction and translation of Mode S raw data, [37] offers a detailed overview. In this work, the Python library pymodes-opensky [38] is used to automatically extract the data from the Impalla Shell of OpenSky. The necessary inputs are the given aircraft (identified by the ICAO 24-bit address code) and the period of time in UTC in which the information wants to be extracted. If the aircraft was flying during that time, the required dataset is obtained. Specific flights can be found by callsigns combining the information of and additional database that includes the callsign, ICAO 24-bit address code, departure airport, departure time, landing airport and landing time for all the flights for a given day. The acquisition of each of the quantities of interest is explained with more detail below:

1. Mach Number: For the aircraft speed, the Mach number is directly obtained from the BDS-60 codes for approximately each second of flight. It provides a more accurate vision of the aircraft speed than by using the TAS.

2. Altitude: Regarding the aircraft altitude, this is directly provided by the ADS-B data. The change in altitude during cruise is strongly conditioned by ATC, as aircraft do not always follow the optimum altitude required for maximum performance. Eastbound flights follow odd flight levels, while westbound flights follow even flight levels. From the altitude, using standard atmosphere asusmptions [35], the freestream pressure, density and viscosity are found. As a result, in combination with the Mach number, the Reynolds number of the aircraft can be directly obtained.

3. Lift Coefficient: The most difficult calculation is the determination of the aircraft weight in flight. This takes into account many assumptions as well as engineering knowledge from the designers. First, aircraft weight can be assumed to exponentially decrease following Breguet equation between take-off and landing. Take off weight includes empty weight (publicly available), fuel weight and payload, which entails an assumption in the number of passengers and cargo. Required fuel weight is obtained for a given mission according aircraft type, departure and destination airports, accounting as well for reserve weight. Landing weight is equal to take-off weight minus the consumed fuel. Assuming level flight in cruise, the lift is equal to the current weight, and can be then directly obtained at each instant according to the Mach number and altitude (air density).

$$C_{L,i} = \frac{W_i g}{0.5 \rho V^2 S_{ref}} = \frac{W_i g}{0.5 \gamma M^2 P S_{ref}} \tag{11}$$

As a result, the required operational conditions for all flights for a given flight route and airliner can be automatically obtained for a period of time. The process is summarized in Figure 4. In that example, the flight data for A320 for the same flight route (callsign) operated in Europe is extracted for a month. Figure 4a shows the Mach number vs time, where the difference in colours correspond to different days. The Mach number is recorded from take-off to landing. Note the variability in the flight duration and in the landing time. From the data, cruise information is filtered according to constant flight level taking into account the altitude, as shown in Figure 4b. For each individual flight, a Kernel Density Estimator is performed to obtain the individual probability density functions (PDFs) of the Mach, as shown in Figure 4c. This already shows how there is a considerable change in speed from flight to flight. Finally, all individual PDFs can be combined into a single PDF which characterizes the distribution of the Mach for a given callsign and airliner (flight number) as it appears in Figure 4d. In that case, the PDF is centred around Mach 0.78, the official cruise point of A320.

4.2 Proposed Approach

For our study, the interested lies in the performance of A330 aircraft, which strongly resemble the characteristics of the XRF1 configuration. In particular, the performance of all the A330 flights operated by five major European carriers is extracted and analyzed for the months of July and August of 2019. Only flights covering continental

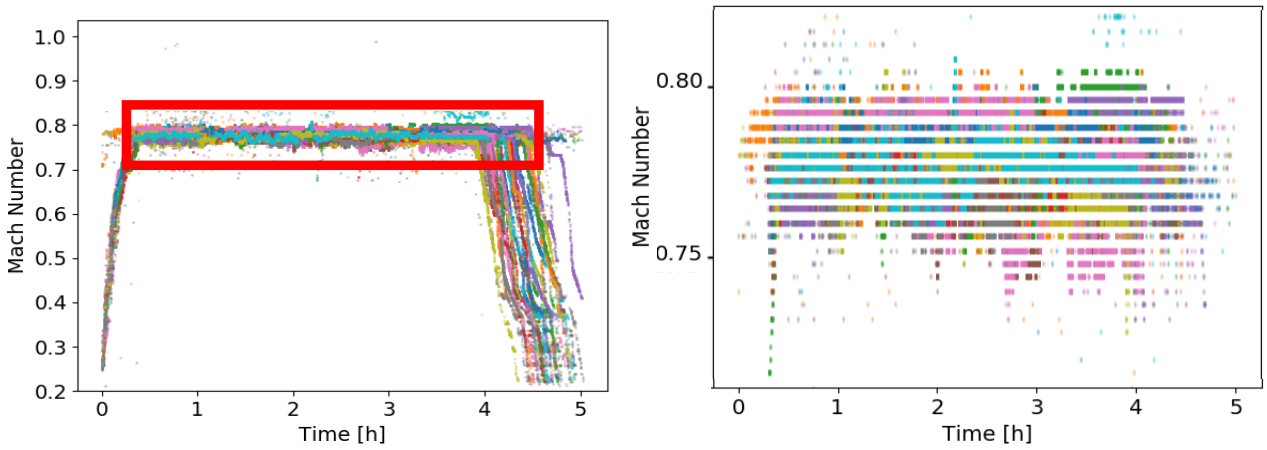

(a) Mach vs time for several flights

(b) Filtered cruise Mach vs time for several flights

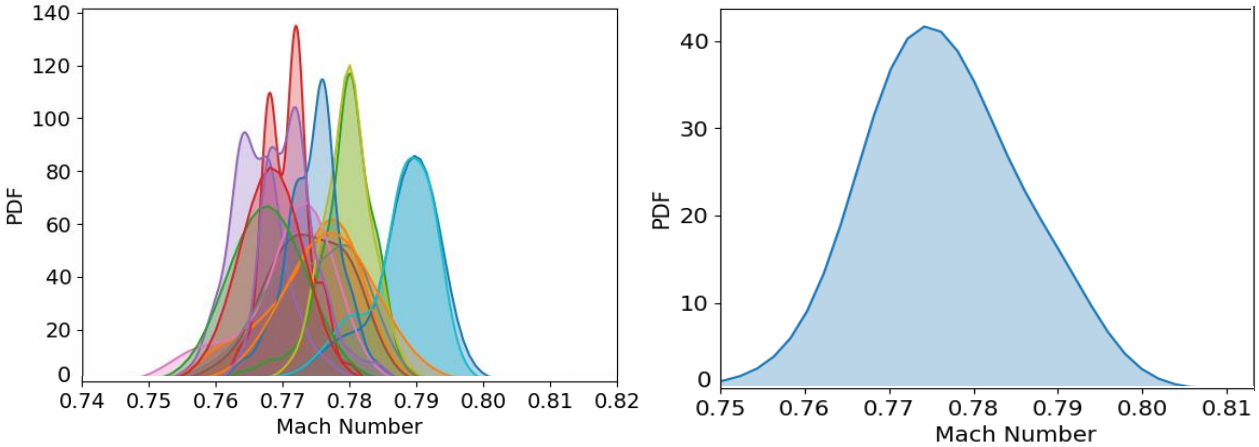

(c) PDF of Mach for individual flights

(d) Combined PDF of Mach for given flight route

Figure 4 – Different steps to obtain the PDF of Mach number for a given flight route

Europe and middle East are selected, as these are the locations with most receivers. An additional table provides for any given day information for the flights for each of the aircraft of interest: callsign (flight number), first seen, last seen, departure airport and origin airport. This provides some clarity and filtering in the large database, and make sure that the flight data belongs only to the desired aircraft and flight route.

A total of 2692 flights are gathered and analysed, corresponding to 165 different callsigns (flight routes), leading to an average of 16 flights per call signs. The data can be summarized in Figure 5. For each individual flight, its average cruise lift coefficient is represented vs its average cruise Mach number. The colours correspond to the different airliners (in this case A, B, C, D and E). Both lift coefficient and Mach number data lies within the expected operating bounds. The cloud of points is centred around the cruise point of the A330, as shown by the red start. From here, it is clear that only a multi-point representation (blue stars) is not enough to characterize the performance of the aircraft.

As in this case the interest lies in the specific retrofit of an array of SCB for a given flight route, the individual flights are collapsed by callsigns. The focus is primarily shifted to the Mach number, as this is the main parameter that influences the shock wave location. Figure 6 shows standard deviation of the cruise Mach vs the average cruise Mach for the individual callsigns. There is a correlation in the flight speed with the airline type by looking at the cluster of points. According to operational and cost requirements, some airliners may decide to fly faster or slower. In addition, two regions can be observed: routes operated at lower speed but with a high variability, and another where the average speed is larger than the cruise point with a lower variability. The later case is of special interest when retrofitting shock control bumps. As a result, the callsign (flight route) R2-R1 of airliner A, as well as its corresponding return flight, R1-R2, are selected as test cases for the design of shock control bumps. This route is operated at considerable higher freestream velocities than the original cruise point, and in this case, the retrofit of a fixed SCB would be attractive.

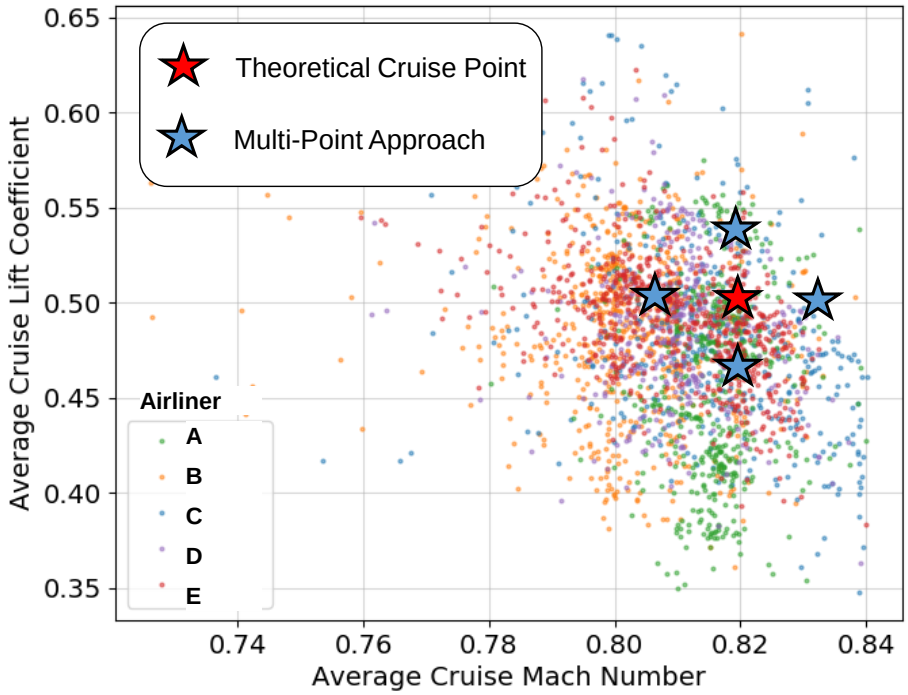

Figure 5 – Average cruise lift coefficient vs average cruise Mach number for A330 flights from 5 different airliners gathered through the OpenSky network

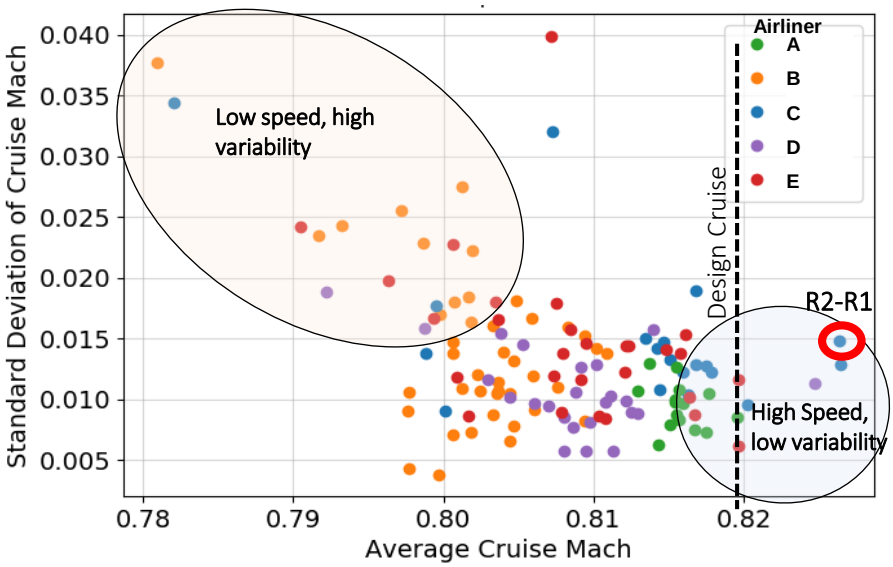

Figure 6 – Standard deviation of cruise Mach number vs average cruise Mach number for A330 callsigns gathered through the OpenSky network

The probability density function (PDF) of the operational uncertainties for the return route is shown in Figure 7. As the operating point of the XRF1 ($M = 0.83$) is not exactly the one of the A330 ($M = 0.82$), this PDF is non-dimensionalized and centered along the XRF1 cruise point. This enables the transfer of uncertainties from the A330 to the XRF1. Uncertainties in lift coefficient and altitude are kept the same. As shown, the lift is centered in $C_L = 0.5$, the cruise lift coefficient of the XRF1, and deviations follow from operational requirements in flight. Regarding altitude, most of the flights occur between FL 370 (for eastbound flights), and FL 400 (for westbound flights).

Based on these uncertainties, the flight conditions for the multi-point optimization represent a five-point stencil in Mach and lift coefficient, centred in cruise point, following state-of-the-art formulations [39]. These are shown in Table 2. In this case, the altitude is kept constant.

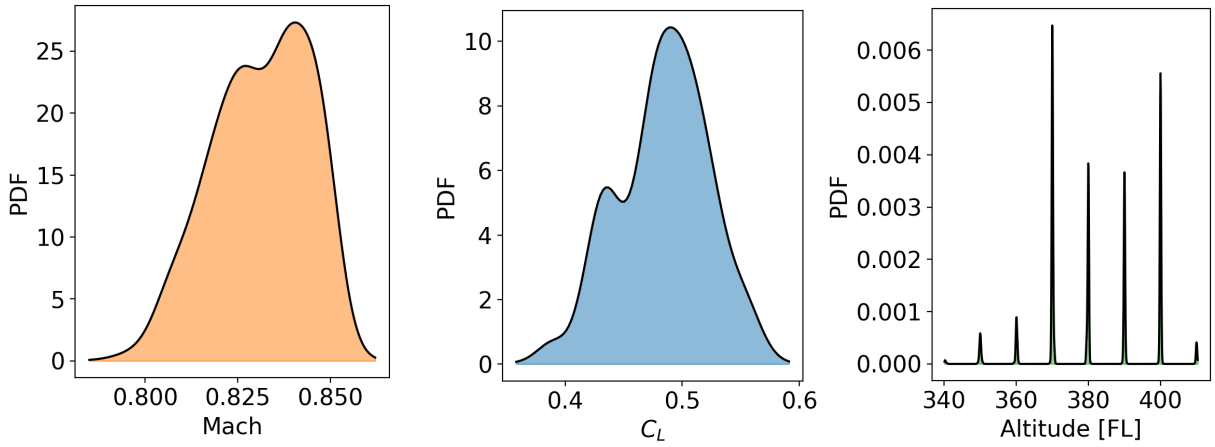

(a) Mach number (b) Lift coefficient (c) Flight altitude

Figure 7 – Parametrization of operational uncertainties for the XRF1 configuration according to R2-R1/ R1-R2 return route

Table 2 – Multi-point flight conditions for the XRF1 configuration

Flight Condition Number	Mach, M	Lift coefficient, C_L	Altitude, [FL]	Weight, w_i
1	0.83	0.5	380	0.3
2	0.83	0.48	380	0.15
3	0.83	0.52	380	0.15
4	0.81	0.5	380	0.15
5	0.83	0.5	380	0.15

4.3 Strengths and Limitations of current approach

The use of surveillance data is the best approach to model realistic operational uncertainties for robust optimization. However, this new approach comes with limitations. First, the data is limited to areas with ground stations, as there is a lack of data from the middle of the oceans or unpopulated areas. Second, the Mach number is provided with limited decimal points, and some postprocessing is necessary to obtain smooth PDFs. The choice of the proper bandwidth for the kernel density estimation is also not trivial. However, the level of accuracy is enough for the present analysis. Third, as previously explained, the lift coefficient is obtained taking into consideration some assumptions in the weight of the aircraft. Fourth, the lift coefficient is assumed to be independent of Mach number and Altitude. Based on initial estimates, a weak correlation may exist, but in practice the independence can be maintained. This is still a better approach than considering uncertainties in the angle of attack. Finally, the addition of more data and the combination with other sources such as flight data recorder will improve the model accuracy.

5. Results

In this section the optimization results are introduced. First the deterministic optimum is found through gradient-based optimization. Then the UQ methods are validated in the baseline wing. Finally, the different optimal robust configurations are presented and analysed with more detail.

5.1 Deterministic Optimization

The deterministic problem is based on the retrofit of a shock control bump at cruise conditions ($M = 0.83$, $C_L = 0.5$, $FL = 380$) under no uncertainty. Represents the state of the art in (deterministic) aerodynamic shape optimization. To investigate the influence in the number of the shock control bumps, three different arrays are optimized with 9, 12 and 15 bumps.

The optimization history of the gradient-based optimization for the three cases is shown in Figure 8a. The objective function is normalized by the drag of the clean wing, $C_{D,0}$. At each iteration, a full CFD solution and 2 adjoint evaluations are required to obtain the drag and gradients with respect to the design parameters. The starting

point corresponds to the middle of the bounds of table 1, leading to $C_D/C_{D,0} = 1.2$ (outside of the chart). From this arbitrary configuration, the optimizer is able to quickly find the optimum array of shock control bumps that minimizes the drag, compared to the clean wing. For the three cases the optimizer needs 28 to 32 iterations to converge. It can be appreciated that the number of bumps has a small influence in the final reduction in drag. The difference is less than 0.5% in drag reduction between the best configuration (12 bumps) and the worst (15 bumps). The array of 12 bumps is able to decrease the drag of the baseline wing by 6.94%. For the robust optimization, 12 bumps (84 design parameters) will also be optimized. The distribution and height of shock control bumps is shown in Figure 8b for the three optimum configurations. In the three cases, the highest bumps originate near the wing root. It appears that there is an optimum spanwise height distribution that is independent on the number of bumps. This is only function of the shock strength

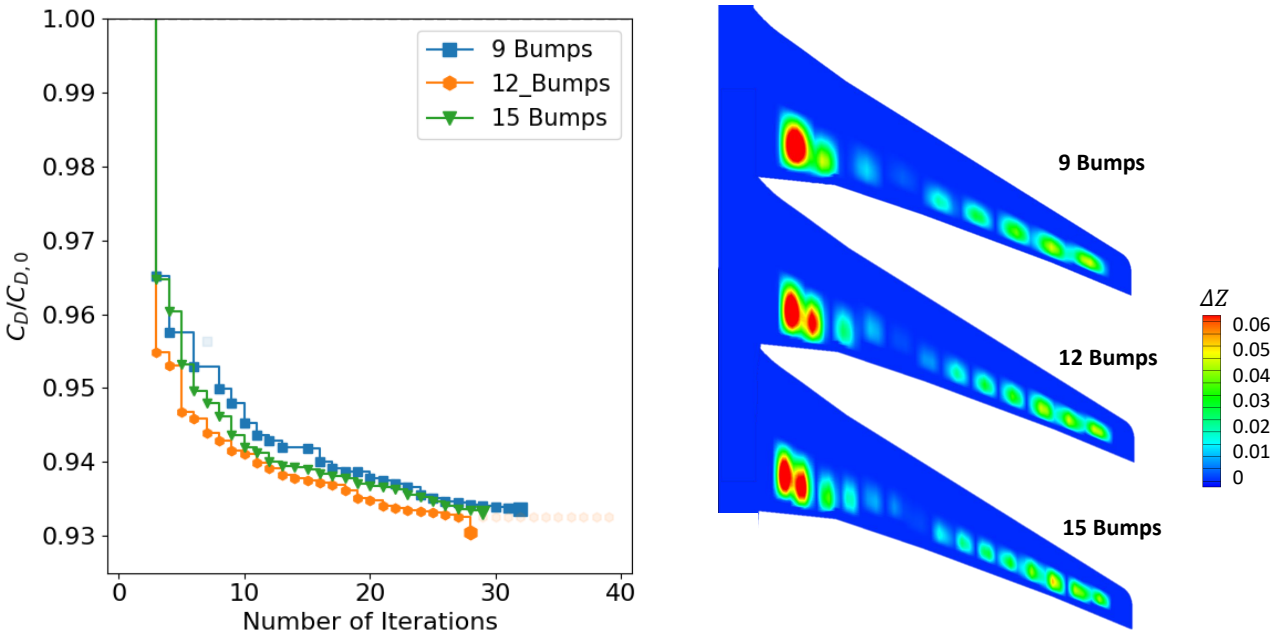

(a) Optimization convergence for the configuration with 9, 12 and 15 bumps

(b) Optimum array for 9, 12 and 15 bumps. The contour represents the bump height w.r.t. clean wing

Figure 8 – Comparison between configurations with 9, 12 and 15 bumps

The configuration with 12 bumps is analysed with more detail. In this case, as shown in Figure 9, the array of bumps is able to mitigate the normal shock wave over the upper surface of the wing, compared to the clean wing, decreasing wave drag. Instead of a sudden change in pressure, the array of shock control bumps has a smoother (more isentropic) pressure change. Looking at different cross section in Figure 10, the normal shock wave present in the clean wing is replaced by an isentropic compression wave at 20%, 40% and 60% of the wingspan for the wing with the retrofitted bumps. In the outboard wing, at 80% of the wing, a double shock is present, phenomena commonly seen when retrofitting shock control bumps [19] to airfoils. As a result, the wave drag is reduced.

The change in the shock wave strength can be qualitatively visualized in Figure 11 for the clean and optimized wing. The shock wave contours have been obtained according to the normal Mach number-based shock detection method [40]. While the baseline wing presents a continuous shock across its upper surface, the wing with the array of shock control bumps is able to mitigate in the chord and the tip, and completely remove it through the mid-span.

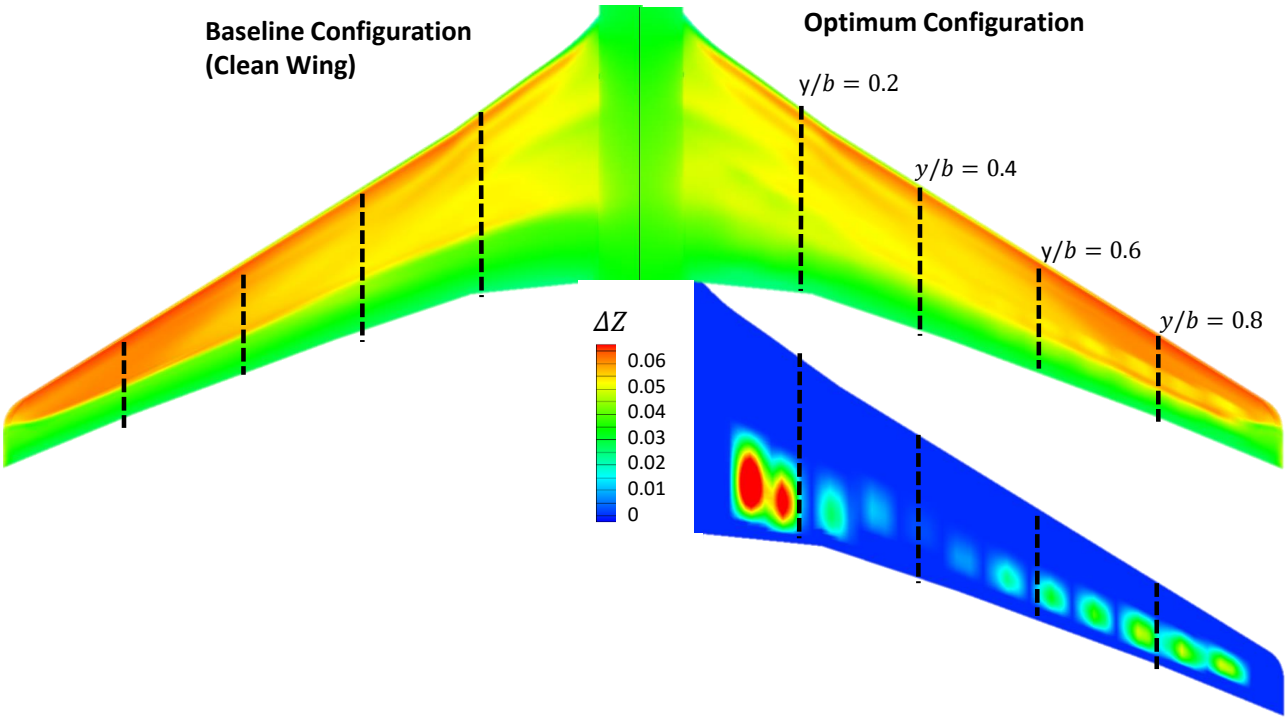

Figure 9 – Contours of pressure coefficient distribution over the upper surface of the wing for the baseline (clean) wing and the optimum retrofitted with 12 bumps

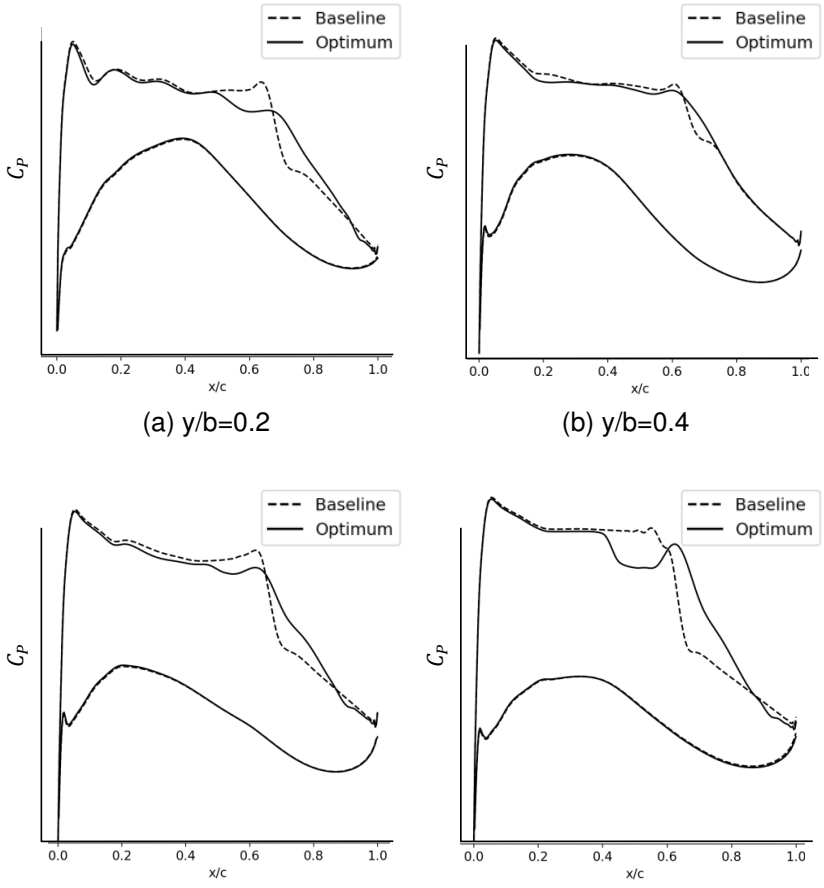

(a) y/b=0.2 (b) y/b=0.4

(c) y/b=0.6 (d) y/b=0.8

Figure 10 – Pressure coefficient for baseline and optimum configurations at different longitudinal cross-sections

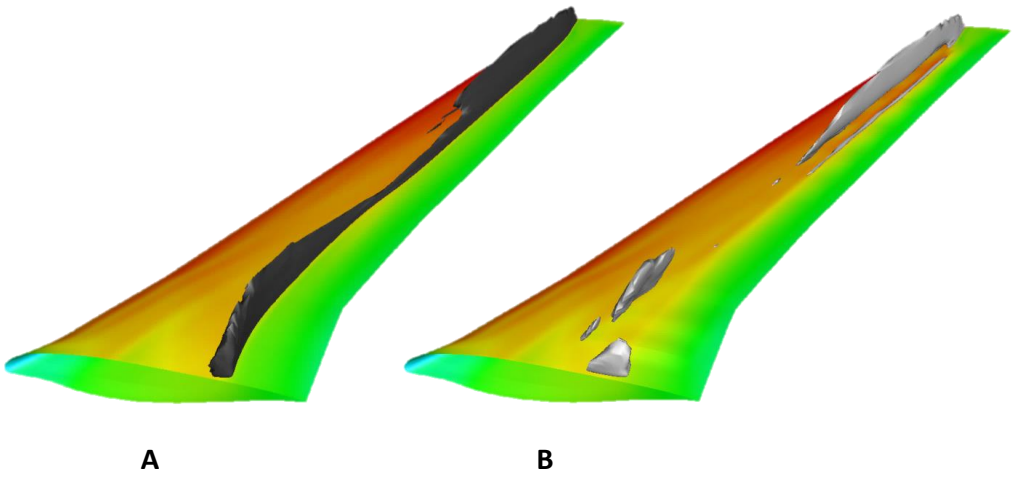

Figure 11 – Shock wave contours according to the normal Mach number shock detection method for baseline wing (A) and wing with optimum SCB array (B)

5.2 Uncertainty Quantification

For validation of the UQ approach, the baseline wing (no bumps) is evaluated under the uncertainties previously introduced in Figure 7. Reference statistics are obtained building the surrogate model with 200 quasi Monte Carlo samples. Using 22 DoE samples and 3 additional samples following the infill criteria, the mean can be obtained within a relative error of 0.1%, while the standard deviation (a much smaller quantity), is obtained within a 0.7% error. These estimations are accurate enough to perform robust optimization and come up with meaningful comparisons.

The mean and standard deviation of the pressure field over the wing is shown in Figure 12. These are obtained by combining 80 random snapshots of the solution field, and computing the mean/standard deviation for each mesh point. The mean field provides an estimate of the expected pressure field under random operational conditions. On average, a strong shock wave is present over the upper surface of the wing. The standard deviation field indicates the variability of the shock wave, as well as its strength. The variability is larger in the wing tip than at the wing root.

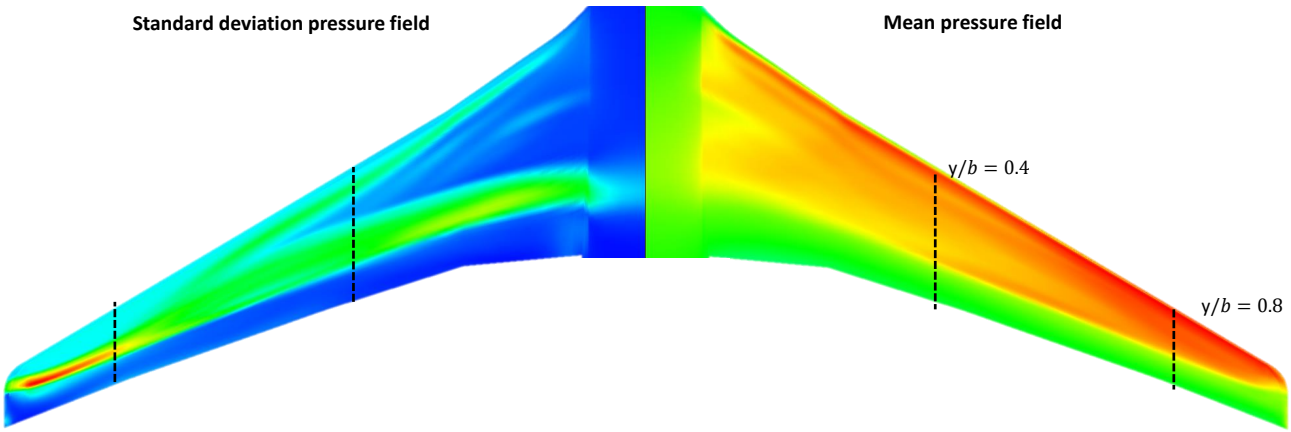

Figure 12 – Mean and standard deviation pressure field under operational uncertainties

For a more detailed understanding of the flow field, realizations of the pressure distribution over the wing are shown in Figure 13 for two cross sections of the wingspan: $y/c = 0.4$ and $y/c = 0.8$. In these two locations the displacement of the shock wave location over the upper surface of the wing can be appreciated as highlighted in red. This justifies the need of robust optimization. A robustly designed array of shock control bumps should be able to better deal with the variability of the shock location than one optimized taking into account only one realization (the design point).

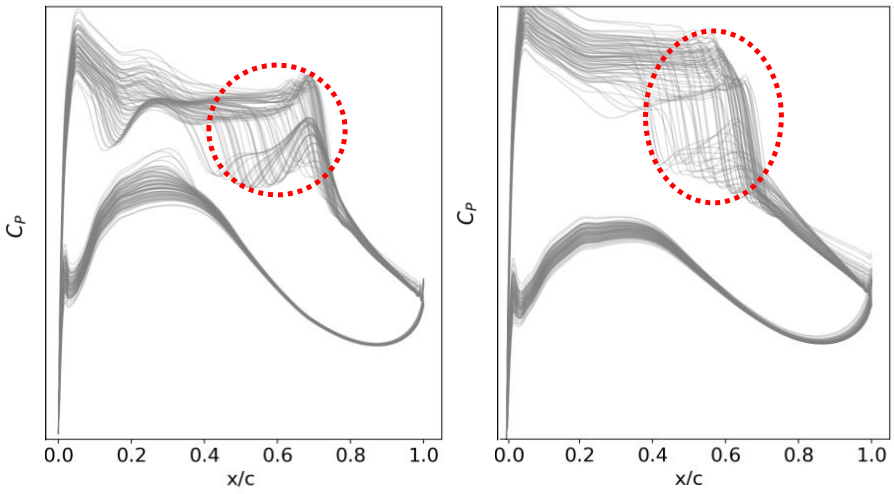

(a) y/b = 0.4 (b) y/b = 0.8

Figure 13 – Realizations of surface pressure coefficient at two different cross sections for the clean wing. In red, the variability in the shock over the upper surface is highlighted

5.3 Robust Optimization

The robust optimization is performed through the gradient-based robust optimization framework. Figure 14 shows the optimization convergence history for the optimization of the mean, Figure 14a, and for the optimization of mean and standard deviation with equal weights, Figure 14b. In both cases the objective function has been normalized by the performance of the clean wing. The optimum solutions are found after 27 and 30 iterations respectively. At each iteration, 23 to 25 CFD and adjoint evaluations are required to accurately obtain the statistics and its gradients. As a result, to find a robust optimum, and order of 600 to 700 CFD + adjoint evaluations are required. It can be appreciated that the statistics of the gradients are accurately obtained, as the optimizer is able to decrease the objective function at each iteration of the optimization. In the case of the optimization of the mean, the average drag is decreased by 3.22%. This is significant from an operational point of view and motivates both the increase in computational cost w.r.t. deterministic optimization, as well as the attractiveness of robustly retrofitted shock control bumps to existing aircraft.

The results of the configurations of interests are summarized in the Pareto front of the mean and standard deviation of drag in the Figure 15. The figure should be read together with table 3. A deterministic optimization of an array of shock control bumps is able to decrease both mean and standard deviation of the drag (1.23% and 14.99% respectively), when realistic uncertainties are present, compared to the clean wing. As expected, a multi-point formulation is able to further decrease the average drag by 2.04%, as different flight conditions were considered during the optimization. However, an extra one percent reduction in the average drag can be achieved with a fully robust formulation compared to the multi-point. This leads towards a 3.22% reduction in average drag when choosing the robust optimization. The ability of evaluating statistical measures directly during the optimization provides a key advantage in this case. Another interesting option is to equally weight mean and standard deviation. The resulting configuration (purple triangle), is able to decrease the standard deviation by 31.4% instead of the 12.5% decrease of obtained by the configuration that only minimized the mean. This is a reduction of the variability by a factor of two. The price to pay is a slight increase in average performance. Still, this configuration is able to improve both mean and standard deviation w.r.t. the multi-point optimum.

The violin plot of Figure 16 shows the symmetric PDF of the normalized drag coefficient for each configuration. The mean value is shown in a white circle, the performance at nominal conditions is represented by the red star, and different quantiles are shown by the superimposed box plot. The violin plot can be used to compare the performance between different configurations. The geometry for each array of SCB is also shown at the top of the Figure. The clean wing (blue PDF), has the largest variability and average drag. The deterministic optimum (orange), reduces the variability and average performance, but also has a thinner tail towards the lowest values of drag. This is not desired as it means that flight conditions that led towards lower values of drag in the clean wing, are being now penalized by the shock control bumps, as these were designed only for a flight condition. The multi-point optimum (green PDF) behaves similarly as the deterministic optimum, although it further reduces

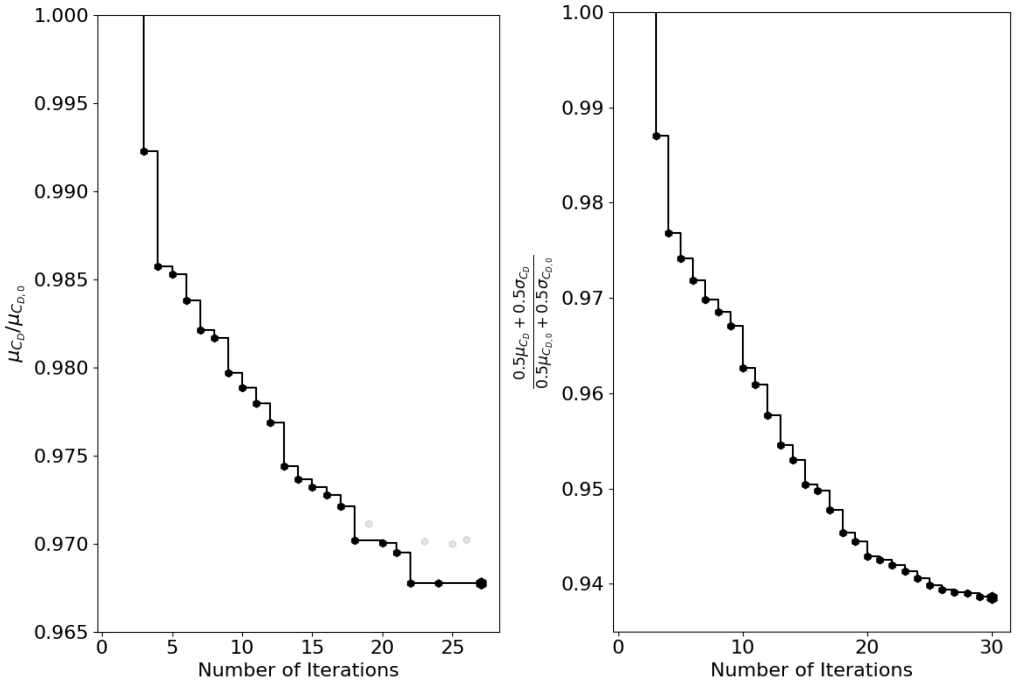

(a) $J^* = \mu_{C_D}$ (b) $J^* = 0.5\mu_{C_D} + 0.5\sigma_{C_D}$

Figure 14 – Robust optimization convergence history

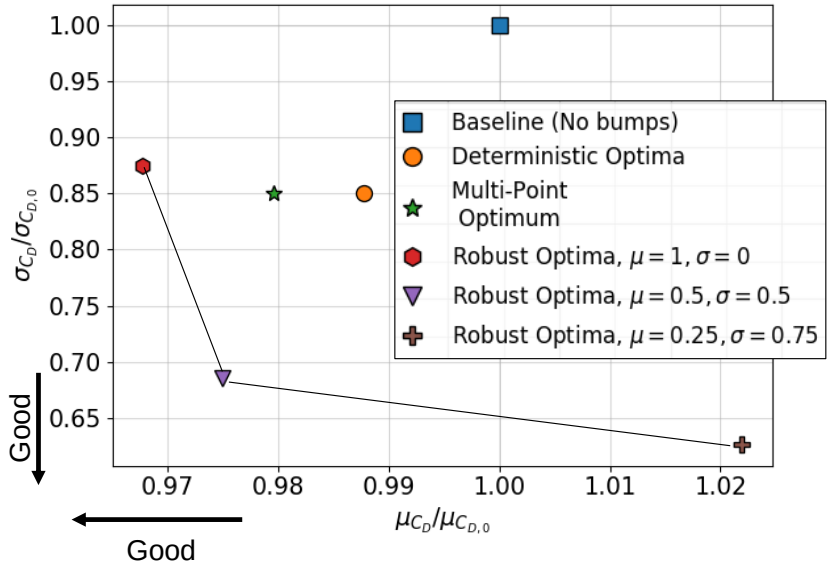

Figure 15 – Pareto front of mean vs standard deviation of dimensionless drag coefficient for different configurations

the average drag. The bump height is similar to the deterministic configuration, although these bumps are closer together. The robust optimum with focus on the mean (red PDF) presents the lowest average drag. The lower tail of the PDF is thicker and extends more towards the lower values of the drag compared to the other configurations. The bump geometry is differentiated, clearly showing the differences between deterministic and robust optimum. The configuration with same weighting in mean and standard deviation (purple PDF) leads to the lowest 95% quantile of the drag. This is achieved by mitigating the stronger shock waves at freestream velocities and lift coefficients higher than the cruise point. As a result, all the shock control bumps are higher (the highest the SCB, the most effective against stronger shocks). Finally, the configuration with more weighting in standard deviation (brown PDF), is able to decrease the standard deviation by an excessive increase in average performance. This configuration is not competitive enough compared to the two previous configurations. Indirectly, for the

deterministic optimum, there is a difference between nominal conditions (star) and the average performance (white dot). This difference is reduced for the robust optimum with focus on the mean (red PDF). In this case, the drag at nominal conditions and the average drag are close together. This could be another interpretation of robustness: under uncertainties, nominal and average performance are similar.

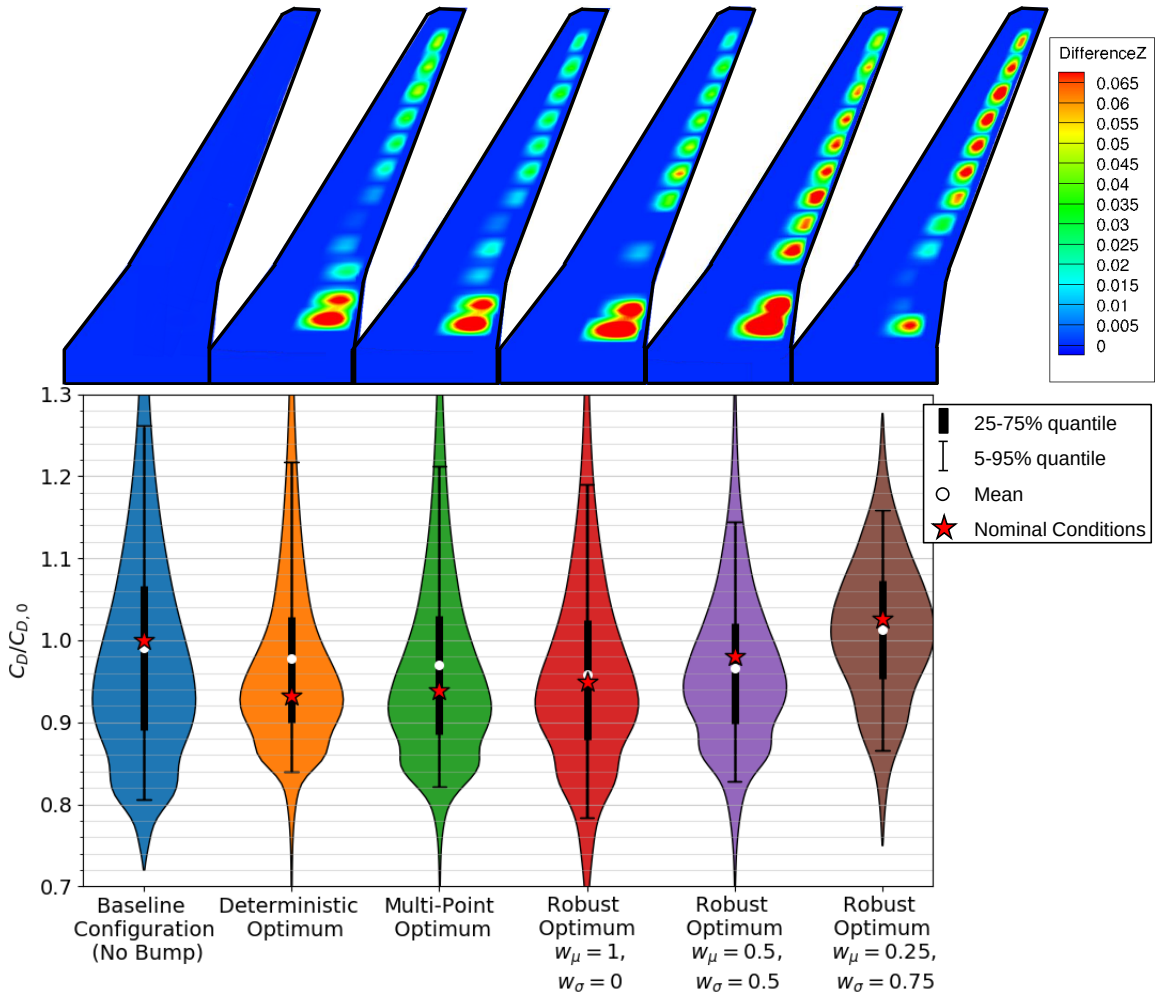

Figure 16 – Violin Plot of the drag coefficient for the configurations of interest. Corresponding bump geometries on top

Table 3 – Decrease in average and standard deviation of the drag w.r.t. clean wing

		Decrease in average drag, μ_{C_D}	Decrease in std. deviation of drag, σ_{C_D}
Deterministic Opt.	●	1.23%	14.99%
Multi-Point Opt.	★	2.04%	14.94%
Robust Opt., $\mu = 1, \sigma = 0$	⬢	3.22%	12.52%
Robust Opt., $w_\mu = 0.5, w_\sigma = 0.5$	▽	2.5%	31.42%

6. Conclusions

The robust design of 3D shock control bumps to the XRF1 is a challenging test case not only due to the non-linearity of the problem involving shock waves, but also due to the high-dimensionality of the design space (in this case 84 design parameters were optimized). In addition, the optimum solution must be achieved within a reasonable CPU time due to the expensive computational cost associated to each CFD and adjoint simulation. The retrofit of an array of fixed shock control bumps to current aircraft is a feasible solution to reduce wave drag. As shown in the deterministic, single-point optimization, the optimizer is able to find from an arbitrary configuration,

the optimum array of shock control bumps that minimizes the drag of the XRF1 by 6.94% compared to the clean wing. The exact number of bumps has a small influence in the final performance. The optimized arrays of shock control bumps are able to decrease the strength of the shock wave over the upper surface of the wing reducing wave drag.

Realistic uncertainties in the Mach number, lift coefficient and aircraft altitude can be obtained from aircraft surveillance data using the OpenSky Network. The presented approach can effectively characterize PDF of the Mach number, lift coefficient and Altitude at different levels: individual flights, flight routes, airliners and aircraft type. These can be used together with an efficient gradient-based robust design methodology to come up with more robust aircraft. This framework is able to find the robust optimum array of shock control bumps within a realistic number of function evaluations. In overall, a reduction in average drag of 3.2% is achieved compared to the clean wing. The robust optimum configurations outperform those obtained through single-point and multi-point optimization techniques, showcasing the benefits of a probabilistic formulation for the retrofit of shock control bumps.

7. Copyright Statement

8. Acknowledgments

This work is funded by the European Commission's H2020 programme, through the UTOPIAE Marie Curie Innovative Training Network, H2020-MSCA-ITN-2016, Grant Agreement number 722734.

References

[1] J. E. Green. Civil aviation and the environment – the next frontier for the aerodynamicist. *The Aeronautical Journal*, 110(1110):469–486, aug 2006.

[2] S.N. Skinner and H. Zare-Behtash. State-of-the-art in aerodynamic shape optimisation methods. *Applied Soft Computing*, 62:933–962, jan 2018.

[3] Gaetan K. W. Kenway and Joaquim R. R. A. Martins. Multipoint aerodynamic shape optimization investigations of the common research model wing. *AIAA Journal*, 54(1):113–128, jan 2016.

[4] Rhea P. Liem, Gaetan K. W. Kenway, and Joaquim R. R. A. Martins. Multimission aircraft fuel-burn minimization via multipoint aerostructural optimization. *AIAA Journal*, 53(1):104–122, jan 2015.

[5] Jichao Li and Jinsheng Cai. Massively multipoint aerodynamic shape design via surrogate-assisted gradient-based optimization. *AIAA Journal*, 58(5):1949–1963, may 2020.

[6] Rhea P. Liem, Joaquim R.R.A. Martins, and Gaetan K.W. Kenway. Expected drag minimization for aerodynamic design optimization based on aircraft operational data. *Aerospace Science and Technology*, 63:344–362, April 2017.

[7] Getting to grips the cost index. Technical Report Issue II - May 1998, Airbus Customer Services.

[8] H. Ogawa, H. Babinsky, M. Pätzold, and T. Lutz. Shock-wave/boundary-layer interaction control using three-dimensional bumps for transonic wings. *AIAA Journal*, 46(6):1442–1452, jun 2008.

[9] Benedikt König. *Shock control bumps on transonic transport aircraft*. PhD thesis, Universität Stuttgart, 2013.

[10] P.R. Ashill, J.L. Fulker, and J.L. Shires. A novel technique for controlling shock strength of laminar-flow airfoil sections. In *Proceedings of the 1st European Forum on Laminar Flow Technology*, pages 175–183, Hamburg, 1992.

[11] Egon Stanewsky, Jean Délery, John Fulker, and Paolo de Matteis. Synopsis of the project euroshock ii. In Egon Stanewsky, Jean Délery, John Fulker, and Paolo de Matteis, editors, *Drag Reduction by Shock and Boundary Layer Control*, pages 1–124, Berlin, Heidelberg, 2002. Springer Berlin Heidelberg.

[12] A.R McGowan. Avst morphing project research summaries in fiscal year 2001. Technical Report nasa tm-2002-2 11769, NASA, August 2002.

[13] P. J. K. Bruce and H. Babinsky. Experimental study into the flow physics of three-dimensional shock control bumps. *Journal of Aircraft*, 49(5):1222–1233, sep 2012.

[14] D. S. Lee, J. Periaux, E. Onate, L. F. Gonzalez, and N. Qin. Active transonic aerofoil design optimization using robust multiobjective evolutionary algorithms. *Journal of Aircraft*, 48(3):1084–1094, may 2011.

[15] Martin Paetzold, Thorsten Lutz, Ewald Kramer, and Siegfried Wagner. Numerical optimization of finite shock control bumps. In *44th AIAA Aerospace Sciences Meeting and Exhibit*. American Institute of Aeronautics and Astronautics, jan 2006.

[16] P. J. K. Bruce and S. P. Colliss. Review of research into shock control bumps. *Shock Waves*, 25(5):451–471, oct 2014.

[17] Edward R. Jinks, Paul J. Bruce, and Matthew J. Santer. Adaptive shock control bumps. In *52nd Aerospace Sciences Meeting*. American Institute of Aeronautics and Astronautics, jan 2014.

[18] Klemens Nuebler, Thorsten Lutz, Ewald Kraemer, Simon Colliss, and Holger Babinsky. Shock control bump robustness enhancement. In *50th AIAA Aerospace Sciences Meeting including the New Horizons Forum and Aerospace Exposition*. American Institute of Aeronautics and Astronautics, jan 2012.

[19] Christian Sabater and Stefan Goertz. An efficient bi-level surrogate approach for optimizing shock control bumps under uncertainty. In *AIAA Scitech 2019 Forum*. American Institute of Aeronautics and Astronautics, jan 2019.

[20] Christian Sabater and Stefan Görtz. *Gradient-Based Aerodynamic Robust Optimization Using the Adjoint Method and Gaussian Processes*, pages 211–226. Springer International Publishing, Cham, 2021.

[21] Andrei Merle, Arthur Stueck, and Arne Rempke. An adjoint-based aerodynamic shape optimization strategy for trimmed aircraft with active engines. In *35th AIAA Applied Aerodynamics Conference*. American Institute of Aeronautics and Astronautics, June 2017.

[22] Gaetan K. Kenway and Joaquim R. R. A. Martins. Aerodynamic shape optimization of the CRM configuration including buffet-onset conditions. In *54th AIAA Aerospace Sciences Meeting*. American Institute of Aeronautics and Astronautics, January 2016.

[23] Michael B Giles and Niles A Pierce. An introduction to the adjoint approach to design. *Flow, turbulence and combustion*, 65(3-4):393–415, 2000.

[24] Regis Duvigneau. Aerodynamic shape optimization with uncertain operating conditions using metamodels. resreport RR-6143, INRIA, 2007.

[25] Alexander I.J. Forrester and Andy J. Keane. Recent advances in surrogate-based optimization. *Progress in Aerospace Sciences*, 45(1-3):50–79, jan 2009.

[26] Daigo Maruyama, Dishi Liu, and Stefan Goertz. Surrogate model-based approaches to UQ and their range of applicability. In *Uncertainty Management for Robust Industrial Design in Aeronautics*, pages 703–714. Springer International Publishing, jul 2018.

[27] Zhong-Hua Han, Stefan Goertz, and Ralf Zimmermann. Improving variable-fidelity surrogate modeling via gradient-enhanced kriging and a generalized hybrid bridge function. *Aerospace Science and Technology*, 25(1):177–189, mar 2013.

[28] Richard Dwight and Zhong-Hua Han. Efficient uncertainty quantification using gradient-enhanced kriging. In *50th AIAA/ASME/ASCE/AHS/ASC Structures, Structural Dynamics, and Materials Conference*. American Institute of Aeronautics and Astronautics, may 2009.

[29] D Kraft. A software package for sequential quadratic programming. Technical Report DFVLR-FB 88-28, DLR German Aerospace Center – Institute for Flight, 1988.

[30] Thomas Gerhold. Overview of the hybrid RANS code TAU. In *MEGAFLOW - Numerical Flow Simulation for Aircraft Design*, pages 81–92. Springer Berlin Heidelberg, 2015.

[31] Thomas Gerhold and Jens Neumann. The parallel mesh deformation of the DLR TAU-code. In *Notes on Numerical Fluid Mechanics and Multidisciplinary Design (NNFM)*, pages 162–169. Springer Berlin Heidelberg, 2006.

[32] K. Mazaheri and A. Nejati. The multi-point optimization of shock control bump with constant-lift constraint enhanced with suction and blowing for a supercritical airfoil. *Flow, Turbulence and Combustion*, 96(3):639–666, oct 2015.

[33] Yun Tian, PeiQing Liu, and PeiHua Feng. Shock control bump parametric research on supercritical airfoil. *Science China Technological Sciences*, 54(11):2935–2944, sep 2011.

[34] Stefan Goertz, Mohammed Abu-Zurayk, René Liepelt, Jonas Jepsen, Tanja Fuehrer, Richard-Gregor Becker, Julian Scherer, Thiemo Kier, and Martin Siggel. Collaborative multi-level mdo process development and application to long-range transport aircraft. In *Proceedings of the 30th Congress of the International Council of the Aeronautical Sciences (ICAS), Daejeon, South-Korea*, number ICAS Paper 2016-0345. ICAS, 2016.

[35] ICAO. *Manual of the ICAO Standard Atmosphere: extended to 80 kilometres (262 500 feet), Doc7488/3*. International Civl Aviation Organization, 3rd edition, 1993.

[36] Matthias Schafer, Martin Strohmeier, Vincent Lenders, Ivan Martinovic, and Matthias Wilhelm. Bringing up OpenSky: A large-scale ADS-b sensor network for research. In *IPSN-14 Proceedings of the 13th International Symposium on Information Processing in Sensor Networks*. IEEE, apr 2014.

[37] Junzi Sun, Huy Vu, Joost Ellerbroek, and Jacco M. Hoekstra. pyModeS: Decoding mode-s surveillance data for open air transportation research. *IEEE Transactions on Intelligent Transportation Systems*, pages 1–10, 2019.

[38] Junzi Sun and Jacco Hoekstra. Integrating pyModeS and OpenSky historical database. In *Proceedings of the 7th*

OpenSky Workshop 2019, vol 67, pages 63–72. EasyChair, 2019.

[39] Zhoujie Lyu, Gaetan K. W. Kenway, and Joaquim R. R. A. Martins. Aerodynamic shape optimization investigations of the common research model wing benchmark. *AIAA Journal*, 53(4):968–985, April 2015.

[40] David Lovely and Robert Haimes. Shock detection from computational fluid dynamics results. In *14th Computational Fluid Dynamics Conference*. American Institute of Aeronautics and Astronautics, August 1999.